PHYSICAL REVIEW E **69**, 056315 (2004)

Long-term behavior of cooling fluid in a rectangular container

Wenxian Lin[1,2,*] and S. W. Armfield[1]
[1]*School of Aerospace, Mechanical and Mechatronic Engineering, University of Sydney, New South Wales 2006, Australia*
[2]*Solar Energy Research Institute, Yunnan Normal University, Kunming, Yunnan 650092, People's Republic of China*

(Received 23 December 2003; published 28 May 2004)

In this study, the long-term behavior of cooling an initially quiescent isothermal Newtonian fluid in a rectangular container with an infinite length by unsteady natural convection due to a fixed wall temperature has been investigated by scaling analysis and direct numerical simulation. Two specific cases are considered. Case 1 assumes that the cooling of the fluid is caused by the imposed fixed temperature on the vertical sidewall while the top and bottom boundaries are adiabatic. Case 2 assumes that the cooling is caused by the imposed fixed temperature on both the vertical sidewall and the bottom boundary while the top boundary is adiabatic. The appropriate parameters to represent the long-term behavior of the fluid cooling in the container are the transient average fluid temperature $T_a(t)$ over the whole volume of the container per unit length (i.e., the transient area average fluid temperature, as used in the subsequent numerical simulations) at time t and the average Nusselt number on the cooling boundary. A scaling analysis has been carried out which shows that for both cases $\theta_a(\tau)$ scales as $e^{-C(ARa)^{-1/4}\tau}$, where $\theta_a(\tau)$ is the dimensionless form of $T_a(t)$, τ is the dimensionless time, A is the aspect ratio of the container, Ra is the Rayleigh number, and C is a proportionality constant. A series of direct numerical simulations with the selected values of A, Ra, and Pr (Pr is the Prandtl number) in the ranges of $1/3 \leqslant A \leqslant 3$, $6\times10^6 \leqslant \mathrm{Ra} \leqslant 6\times10^{10}$, and $1 \leqslant \mathrm{Pr} \leqslant 1000$ have been carried out for both cases to validate the developed scaling relations. It is found that these numerical results agree well with the scaling relations. The numerical results have also been used to quantify the scaling relations and it is found that $C = 0.645$ and 0.705 respectively for Cases 1 and 2 with Ra, A and Pr in the above-mentioned ranges.

DOI: 10.1103/PhysRevE.69.056315 PACS number(s): 44.25.+f, 47.15.Rq, 47.27.Te, 83.85.Pt

I. INTRODUCTION

Cooling/heating a body of fluid in an enclosure via natural convection with an imposed different temperature or heat flux on the enclosure boundary is widely encountered in nature and in engineering settings, and the understanding of its behavior is of fundamental interest and practical importance. In the past decades, extensive experimental, numerical, and analytical studies have been conducted on this issue, although mainly on the more specific case of a rectangular cavity with differentially heated sidewalls, such as those well documented in Ref. [1] and in the annual literature reviews on heat transfer (see, e.g., Ref. [2]).

The majority of the past studies have been on the short-term behavior of the cooling/heating process, involving either the boundary-layer formation and its evolution on the cooling/heating wall, the traveling wave activities, the stratification established in the enclosure, or the combinations of these features. For example, Sakurai and Matsuda [3] conducted a theoretical investigation into the transient process in an already stratified fluid, revealing the core of the intricate physics involved in the transient adjustment process of a stratified fluid system in response to changes in thermal boundary conditions in a vertical circular cylinder, which was further modified and extended analytically by Jischke and Doty [4], and numerically by Hyun *et al.* [5].

Patterson and Imberger [6] carried out a pioneering investigation of the transient features that occur when the temperatures at the opposing two vertical side walls of a rectangular cavity are impulsively heated and cooled by an equal amount, devising a classification of the development of the flow through several transient flow regimes to one of three steady-state types of flow based on the relative values of Ra, the Rayleigh number, and various combinations of Pr, the Prandtl number, and A, the aspect ratio of cavity. This Patterson-Imberger flow model has since occupied the center stage of research into understanding natural convection in cavities, and numerous investigations subsequently focused on diverse aspects of the model. For example, the numerical studies by Hyun [7] elucidated the flow and temperature structures of the heat-up process of an initially homogeneous fluid in a cylinder with a linearly heated side wall using a finite-difference model and the effect of Pr on heatup of a stratified fluid in an enclosure. Nicolette and Yang [8] made a numerical and experimental investigation into two-dimensional transient natural convection of single-phase fluids inside a completely filled square enclosure with one vertical wall cooled and the other three walls insulated. Otis and Roessler [9] conducted an experimental investigation into the development of stratification of a gas in a cylindrical enclosure and provided experimental support for the existence of internal waves and revealed several time constants that characterize the process. Schladow, Patterson, and Street [10] conducted a series of two- and three-dimensional numerical simulations of transient flow in a side-heated cavity and their simulations generally agree with the results of the scaling arguments [6]. Patterson and Armfield [11] conducted detailed experimental and numerical investigations into the presence of traveling wave instabilities on the vertical-wall

---

[*] Electronic address: wenxian.lin@aeromech.usyd.edu.au
FAX: +61-2-9351-7060

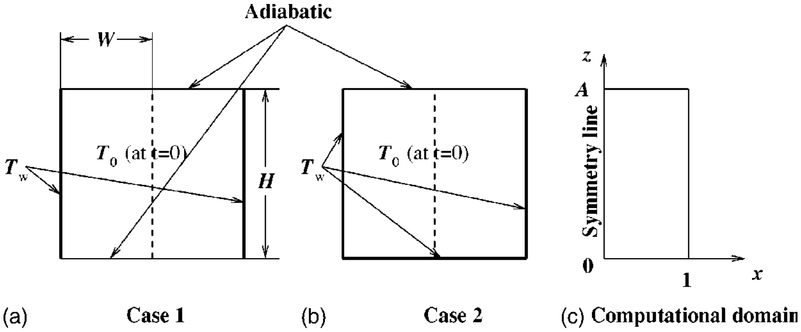

FIG. 1. Schematic depiction of the physical systems and the computational domain.

boundary layers and horizontal intrusions, the existence of a rapid flow divergence in the region of the outflow of the intrusions, and the presence of cavity-scale oscillations caused by the interaction of the intrusion with the opposing vertical boundary layer. Armfield *et al.* [12] made further in-depth studies on the wave and stability properties of the boundary layers in the cavities. Xin and Le Quéré [13] investigated numerically chaotic natural convection in a differentially heated air-filled cavity with adiabatic horizontal walls. Brooker, Patterson, and Armfield [14] conducted a nonparallel linear stability analysis of the vertical boundary layer in a differentially heated cavity. Kwak, Kuwahara, and Hyun [15] conducted a numerical study on the transient natural convective cool-down process of a fluid in a cylindrical container, with emphasis on the flow patterns when the maximum density temperature is experienced.

More recently, the authors carried out a scaling analysis and direct numerical simulation of the transient processes of cooling down and stratifying an initially homogeneous fluid by natural convection in a vertical circular cylinder and in a rectangular container [16–18]. The results show that vigorous flow activities concentrate mainly in the vertical thermal boundary layer along the side wall and in the horizontal region which is the lower part of the domain where the cold intrusion flow is created. The transient flow patterns at the unsteady and quasisteady stages were analyzed, including the activities of the traveling waves in the vertical thermal boundary layer along the side wall, the cold intrusion movements in the horizontal region, and the stratification of the fluid. A scaling analysis was used to characterize the flow evolution at these distinct developmental stages which was quantified by extensive direct numerical simulations under different flow situations in terms of Ra, Pr, and A. The scaling relations were also obtained by the authors [19] for the boundary layer development along a vertical isothermal plate in a linearly stratified fluid with $\mathrm{Pr}>1$. Oliveski, Krenzinger, and Vielmo [20] made a numerical and an experimental analysis of velocity and temperature fields inside a storage tank submitted to natural convection cooling. All these studies have addressed only the short-term behavior of the cooling/heating process, while the study of the long-term behavior is rare, which motivates the current study.

In this study, the long-term behavior of cooling a quiescent isothermal Newtonian fluid in a rectangular container with an infinite length by unsteady natural convection with a fixed lower wall temperature is investigated by a scaling analysis and direct numerical simulation. Specifically, the long-term behavior of the fluid cooling due to the imposed lower fixed temperature on the vertical side wall, with all the remaining boundaries adiabatic; and that due to the imposed fixed lower temperature on both the vertical side wall and the bottom boundary, with the top boundary adiabatic is investigated. In Sec. II, a scaling analysis is carried out to develop the scaling relations to characterize the long-term behavior of the fluid cooling, which is well represented by the transient average fluid temperature in the container and the average Nusselt number(s) on the cooling wall(s). In Sec. III, the governing equations and the numerical methods as well as the meshes used in this study are briefly introduced. The scaling relations are then validated and quantified in Sec. IV by a series of direct numerical simulations with the selected values of A, Ra, and Pr in the ranges of $1/3 \leqslant A \leqslant 3$, $6\times 10^6 \leqslant \mathrm{Ra} \leqslant 6\times 10^{10}$, and $1 \leqslant \mathrm{Pr} \leqslant 1000$. Finally, conclusions are summarized in Sec. V.

II. SCALING ANALYSIS

Under consideration is the long-term behavior of cooling a quiescent isothermal Newtonian fluid in a rectangular container with an infinite length by unsteady natural convection due to the imposed fixed lower wall temperature. The physical systems considered in this study are schematically depicted in Fig. 1. Two cases are considered. Case 1 assumes that the cooling of the fluid is the result of the imposed fixed wall temperature T_w on the vertical side wall while all the remaining boundaries are adiabatic and nonslip. Case 2 assumes that the cooling is due to the imposed fixed temperature T_w on both the vertical side wall and the bottom boundary while the top boundary is adiabatic and nonslip. For both cases, the fluid in the container is initially at rest and at a uniform temperature T_0 ($T_0 > T_w$). It is assumed that the container has an infinite length and the flows are laminar so that two-dimensional flows can be assumed and symmetry allows only one half of the physical domain to be chosen as the computational domain, as shown in Fig. 1(c).

The long-term behavior of the fluid cooling is well represented by the transient average fluid temperature $T_a(t)$ over the whole volume of the container per unit length (i.e., the transient area average fluid temperature, as used in the subsequent numerical simulations) at time t and the average Nusselt number on the cooling wall. In this section, scaling relations will be developed to characterize $T_a(t)$ with the control parameters of the flow, that is, the Rayleigh number Ra, Prandtl number Pr, and the aspect ratio A of the rectangular container, which are defined as follows,

$$\mathrm{Ra}=\frac{g\beta(T_0-T_w)W^3}{\nu\kappa},\quad \mathrm{Pr}=\frac{\nu}{\kappa},\quad A=\frac{H}{W},$$

where g is the acceleration due to gravity, β, ν, and κ are the thermal expansion coefficient, kinematic viscosity, and thermal diffusivity of fluid, and H and W are the height and half-width of the container, respectively.

In this study, the investigation will focus on the flows with $1 \leqslant \mathrm{Pr} \leqslant 1000$, $6\times 10^6 \leqslant \mathrm{Ra} \leqslant 6\times 10^{10}$, and $1/3 \leqslant A \leqslant 3$. For such flows, it is appropriate to assume that ρ, the density of the fluid, is constant, except that appearing in the buoyancy, and c_p, the specific heat of fluid at constant pressure, is also constant.

A. Case 1

In this case, as the fluid cooling is achieved by maintaining a fixed temperature T_w on the vertical side wall while keeping the top and bottom boundaries adiabatic, energy conservation in the container requires that

$$\rho V_c c_p \frac{dT_a(t)}{dt}=-\overline{h_s}A_s[T_a(t)-T_w], \tag{1}$$

where $V_c=2HW$ is the volume of the fluid in the container per unit length, $A_s=2H$ is the surface area of the side wall per unit length, and $\overline{h_s}$ is the average heat transfer coefficient on the side wall. The initial condition for Eq. (1) is as follows:

$$T_a(t)=T_0 \quad \text{at} \quad t=0. \tag{2}$$

Equation (1) can also be written in the following dimensionless form,

$$\frac{d\theta_a(\tau)}{\theta_a(\tau)+1}=-\frac{\overline{h_s}}{\rho c_p V_0}d\tau, \tag{3}$$

in which the dimensionless temperature $\theta_a(\tau)$ and time τ are defined respectively as follows

$$\theta_a(\tau)=\frac{T_a(t)-T_0}{T_0-T_w},\quad \tau=\frac{t}{(W/V_0)}, \tag{4}$$

where V_0 is a characteristic velocity scale of the flow. For unsteady natural convection flow in a cavity, it is a common practice to use $V_0=\kappa \mathrm{Ra}^{1/2}/W$, the velocity scale of the thermal boundary layer thickness [6,16,18], which is also used here. The initial condition (2) becomes

$$\theta_a(\tau)=0 \text{ at } \tau=0. \tag{5}$$

$\overline{h_s}$ in Eq. (1) is calculated by

$$\overline{h_s}=\frac{k\overline{\mathrm{Nu}_s}}{H}, \tag{6}$$

in which k is the thermal conductivity of fluid, and $\overline{\mathrm{Nu}_s}$ is the average Nusselt number on the side wall, which is defined as

$$\overline{\mathrm{Nu}_s}=\frac{1}{A}\int_0^A\left(\frac{\partial\theta}{\partial x}\right)_{x=1}dy, \tag{7}$$

where $(\partial\theta/\partial x)_{x=1}$ is the dimensionless temperature gradient at the vertical side wall, and x and y are dimensionless horizontal and vertical coordinates (nondimensionalized by W), respectively. Hence, Eq. (3) becomes

$$\frac{d\theta_a(\tau)}{\theta_a(\tau)+1}=-\frac{\overline{\mathrm{Nu}_s}}{A\mathrm{Ra}^{1/2}}d\tau, \tag{8}$$

where the relationship $\kappa=k/(\rho c_p)$ has been used.

When $\tau \gg 0$, numerical results show that $\overline{\mathrm{Nu}_s}d\tau$ has the same order as $\tau d\overline{\mathrm{Nu}_s}$, therefore, Eq. (8) can be written as

$$\frac{d\theta_a(\tau)}{\theta_a(\tau)+1}=-\frac{2C_0}{A\mathrm{Ra}^{1/2}}d(\overline{\mathrm{Nu}_s}\tau), \tag{9}$$

where C_0 is a proportionality constant.

As shown in Refs. [17,19], after the full development of the boundary layer on the vertical side wall, the thermal boundary layer thickness δ_s has the following scaling relation with Ra_H,

$$\delta_s \sim \mathrm{Ra}_H^{-1/4}, \tag{10}$$

for $\mathrm{Pr}>1$, where the symbol "$\sim$" denotes "scales to," and Ra_H is the Rayleigh number defined with H, that is,

$$\mathrm{Ra}_H=\frac{g\beta(T_0-T_w)H^3}{\nu\kappa}=\mathrm{Ra}A^3.$$

Therefore, $\overline{\mathrm{Nu}_s}$ should have the following scaling relation with Ra for $\mathrm{Pr}>1$:

$$\overline{\mathrm{Nu}_s}\sim\frac{1}{A}\int_0^A\frac{1}{\delta_s}dy\sim\mathrm{Ra}_H^{1/4}\sim\mathrm{Ra}^{1/4}A^{3/4}. \tag{11}$$

Hence, Eq. (9) has the following solution

$$\theta_a(\tau)=e^{-C_1(A\mathrm{Ra})^{-1/4}\tau}-1, \tag{12}$$

where C_1 is a proportionality constant.

B. Case 2

In this case, as the fluid cooling is achieved by maintaining a fixed temperature T_w on both the side wall and the bottom boundary of the container while keeping the top boundary adiabatic, energy conservation requires that

$$\rho V_c c_p \frac{dT_a(t)}{dt}=-(\overline{h_s}A_s+\overline{h_b}A_b)[T_a(t)-T_w], \tag{13}$$

where $\overline{h_b}$ is the average heat transfer coefficient on the bottom boundary with the surface area per unit length $A_b=2W$. It is assumed that $\overline{h_b}\ll\overline{h_s}$ and the scaling relation (11) is also valid for $\overline{\mathrm{Nu}_b}$, that is,

$$\overline{\mathrm{Nu}_b}\sim\mathrm{Ra}^{1/4}, \tag{14}$$

where $\overline{\mathrm{Nu}_b}$ is the average Nusselt number on the bottom boundary, which is defined as follows

$$\overline{\mathrm{Nu}}_b = \int_0^1 \left(\frac{\partial \theta}{\partial y}\right)_{y=0} dx, \tag{15}$$

in which $(\partial\theta/\partial y)_{y=0}$ is the dimensionless temperature gradient at the bottom boundary. Hence, Eq. (13) can be reduced to an ordinary differential equation similar to Eq. (9) with the same initial condition represented by Eq. (5), which has the following scaling relation

$$\theta(\tau) = e^{-C_2(A\mathrm{Ra})^{-1/4}\tau} - 1, \tag{16}$$

where C_2 is another proportionality constant.

III. GOVERNING EQUATIONS AND NUMERICAL METHOD

A. Governing equations

The two-dimensional unsteady natural convection flow in the container is governed by the Navier-Stokes equations and temperature equation. With the Boussinesq assumption, these governing equations can be written in dimensionless and incompressible form as follows:

$$\frac{\partial u}{\partial x} + \frac{\partial v}{\partial y} = 0, \tag{17}$$

$$\frac{\partial u}{\partial \tau} + \frac{\partial (uu)}{\partial x} + \frac{\partial (vu)}{\partial y} = -\frac{\partial p}{\partial x} + \frac{Pr}{Ra^{1/2}}\left[\frac{\partial^2 u}{\partial x^2} + \frac{\partial^2 u}{\partial y^2}\right], \tag{18}$$

$$\frac{\partial v}{\partial \tau} + \frac{\partial (uv)}{\partial x} + \frac{\partial (vv)}{\partial y} = -\frac{\partial p}{\partial y} + \frac{Pr}{Ra^{1/2}}\left[\frac{\partial^2 v}{\partial x^2} + \frac{\partial^2 v}{\partial y^2}\right] + Pr\theta, \tag{19}$$

$$\frac{\partial \theta}{\partial \tau} + \frac{\partial (u\theta)}{\partial x} + \frac{\partial (v\theta)}{\partial y} = \frac{1}{Ra^{1/2}}\left[\frac{\partial^2 \theta}{\partial x^2} + \frac{\partial^2 \theta}{\partial y^2}\right]. \tag{20}$$

where x, y, u, v, τ, p, and θ are, respectively, the nondimensionalized x coordinate, y coordinate, x—velocity, y—velocity, time, pressure, and temperature.

All the lengths, velocities, time, pressure, and temperature in the governing equations are made dimensionless by W, V_0, W/V_0, ρV_0^2, and $(T-T_0)/(T_0-T_w)$, respectively, where T is the dimensional temperature.

The appropriate initial and boundary conditions are

$$u = v = 0, \quad \theta = 0 \text{ at all } x,y \text{ and } \tau < 0;$$

and

$$u = 0, \quad \frac{\partial v}{\partial x} = 0, \quad \frac{\partial \theta}{\partial x} = 0 \text{ at } x = 0, \quad 0 \leqslant y \leqslant A, \quad \text{on the symmetry line},$$

$$u = v = 0, \quad \theta = -1 \text{ at } x = 1, \quad 0 \leqslant y \leqslant A,$$

$$u = v = 0, \quad \frac{\partial \theta}{\partial y} = 0 \text{ at } 0 \leqslant x \leqslant 1, \quad y = 0 \text{ for Case 1},$$

$$u = v = 0, \quad \theta = -1 \text{ at } 0 \leqslant x \leqslant 1, \quad y = 0 \text{ for Case 2},$$

$$u = v = 0, \quad \frac{\partial \theta}{\partial y} = 0 \text{ at } 0 \leqslant x \leqslant 1, \quad y = A, \quad \tau \geqslant 0.$$

TABLE I. Vertical stretching factors and time steps used in the direct numerical simulations.

Run	Ra	A	Pr	Vertical stretching factor	Time step
1	6×10^{6}	1	7	1.0412	3.5×10^{-4}
2	6×10^{7}	1	7	1.0412	5.5×10^{-4}
3	6×10^{8}	1	7	1.0412	8.7×10^{-4}
4	6×10^{9}	1	7	1.0412	1.4×10^{-3}
5	6×10^{10}	1	7	1.0412	8.7×10^{-4}
6	6×10^{8}	1/3	7	1.0106	1.7×10^{-3}
7	6×10^{8}	1/2	7	1.0205	1.7×10^{-3}
8	6×10^{8}	2	7	1.0705	4.4×10^{-4}
9	6×10^{8}	3	7	1.0650	4.4×10^{-4}
10	6×10^{8}	1	1	1.0412	6.1×10^{-4}
11	6×10^{8}	1	50	1.0412	6.1×10^{-4}
12	6×10^{8}	1	200	1.0412	3.1×10^{-4}
13	6×10^{8}	1	1000	1.0412	2.4×10^{-4}

B. Numerical method

Detailed information about the numerical algorithm and numerical accuracy tests can be found in Refs. [16,17]. Only a brief introduction is presented here.

Due to the large variation in length scales it is necessary to use a mesh that concentrates points in the boundary layer and is relatively coarse in the interior. In this study, the mesh used for all runs of direct numerical simulations is constructed using a stretched grid and has 199 × 199 grid points, which are distributed symmetrically with respect to the half-width and half-height of the computational domain represented by Fig. 1(c). The nearest grid point is located 0.001 from the domain boundaries. Subsequently, the mesh expands at a fixed rate up to $x=y=0.1$ in both x and y directions. After that, the mesh size expansion rate decreases at a rate of 10% until it reaches zero, resulting in a constant coarse mesh in the interior of the domain.

The stretching factor in the x direction is chosen to be 4.12% for all runs but some different values of the stretching factor have been chosen for the runs with $A \neq 1$ in the y direction for constructing the mesh with the same 199 × 199 grid points, as listed in Table I, where the vertical stretching factors and the time steps used in all 13 runs are presented for both cases.

The equations are discretized on a non-staggered mesh using finite volumes, with standard second-order central difference schemes used for the viscous, pressure gradient and divergence terms. The QUICK third-order upwind scheme is used for the advective terms [23]. The second-order Adams-Bashforth scheme and Crank-Nicolson scheme are used for the time integration of the advective terms and the diffusive terms, respectively. To enforce the continuity, the pressure correction method is used to construct a Poisson's equation which is solved using the preconditioned GMRES method. Detailed descriptions of these schemes were given in Ref. [24] and the code has been widely used for the simulation of a range of buoyancy dominated flows (see, e.g., Refs. [11,25,26]).

IV. NUMERICAL RESULTS AND DISCUSSIONS

The purpose of the direct numerical simulations in this study is threefold. First, the scaling relations (12) and (16) are verified by the numerical simulation results with selected values of Ra, A, and Pr in the ranges of $1/3 \leqslant A \leqslant 3$, $6\times 10^6 \leqslant \mathrm{Ra} \leqslant 6\times 10^{10}$, and $1 \leqslant \mathrm{Pr} \leqslant 1000$. Second the proportionality constants C_1 and C_2 in the scaling relations are quantified using these numerical results. Finally, the long-term behavior of the averaged Nusselt numbers and the assumption that $\overline{h_b} \ll \overline{h_s}$, which was made in the scaling analysis, are examined using these numerical results.

The technique for verifying the scaling relations (12) and (16) is first by examining the dependence of these scaling relations on individual control parameters Ra, A, and Pr respectively, which will be achieved by carrying out a series of direct numerical simulations with several selected values of a specific parameter while keeping the other control parameters unchanged with selected values, and then by examining the combined dependence of the scaling relations on all control parameters, which will be achieved by combining the three sets of individual numerical results obtained in the previous step. Specifically, direct numerical simulations with $\mathrm{Ra}=6\times 10^6$, 6×10^7, 6×10^8, 6×10^9, and 6×10^{10} while keeping $A=1$ and $\mathrm{Pr}=7$ unchanged will be carried out to show the dependence of the scaling relations on Ra (runs 1–5); simulations with $A=1/3$, $1/2$, 1, 2, and 3 while keeping $\mathrm{Ra}=6\times 10^8$ and $\mathrm{Pr}=7$ unchanged will be carried out to show the dependence on A (runs 3 and 6–9); and simulations with $\mathrm{Pr}=1$, 7, 50, 200, and 1000 while keeping $\mathrm{Ra}=6\times 10^8$ and $A=1$ unchanged will be used to show the dependence of the scaling relations on Pr (runs 3 and 10–13), respectively.

As theoretically and numerically it needs an infinite time to fully cool down the fluid in the container [that is, to reach exactly $\theta_a(\tau)=-1$], it is necessary to terminate the numerical simulations at some point. In this study, as a general rule, all direct numerical simulations will be terminated when $\tau=\tau_f$, that is when $\theta_a(\tau_f)=-0.99$.

Details of the flow structures during the stages of the start-up and the stratification were reported in Ref. [16–18], which will not be repeated here.

A. Case 1

Figure 2 contains the numerically obtained $\theta_a(\tau)$ for all 13 runs in Case 1 to show the dependence of the scaling relation (12) on each individual control parameter Ra, A, and Pr. Figure 2(a) contains the raw data showing the time series of $\theta_a(\tau)$ for $\mathrm{Ra}=6\times 10^6$, 6×10^7, 6×10^8, 6×10^9, and 6×10^{10} with $A=1$ and $\mathrm{Pr}=7$ unchanged. The scaling relation (12) shows that the dependence of $\theta_a(\tau)$ on Ra goes like $\mathrm{Ra}^{-1/4}$, and the time series of $\theta_a(\tau)$ with this scaling are shown in Fig. 2(b), where it is seen that this scale brings all five sets of data for different Ra together, indicating that $\mathrm{Ra}^{-1/4}$ is the correct dependence of $\theta_a(\tau)$ on Ra in the scaling relation (12). Similarly, Fig. 2(c) contains the raw data showing the time series of $\theta_a(\tau)$ for $A=1/3$, $1/2$, 1, 2, and 3 with $\mathrm{Ra}=6\times 10^8$ and $\mathrm{Pr}=7$ unchanged. The scaling relation (12) shows that the dependence of $\theta_a(\tau)$ on A goes like $A^{-1/4}$, and the time series of $\theta_a(\tau)$ with this scaling are shown in Fig. 2(d), where, again, it is seen that this scale brings all five sets of data for different A together, indicating that $A^{-1/4}$ is the correct dependence of $\theta_a(\tau)$ on A in the scaling relation (12). Figure 2(e) contains the raw data showing the time series of $\theta_a(\tau)$ for $\mathrm{Pr}=1$, 7, 50, 200, and 1000 with $\mathrm{Ra}=6\times 10^8$ and $A=1$ unchanged. The scaling relation (12) shows that there is no dependence of $\theta_a(\tau)$ on Pr, and the overlaying of all five sets of raw data for different Pr presented in Fig. 2(e) clearly demonstrates this feature.

The numerically obtained $\theta_a(\tau)$ is plotted against the full scaling relation $(A\mathrm{Ra})^{-1/4}\tau$ in Fig. 3(a) for all runs in Case 1. The collapse of all sets of data onto a single curve again confirms that the scaling relation (12) is true for Case 1. The specific values of the proportionality constant C_1 for each run, determined by a curve-fitting method with the minimal standard deviation (denoted as sd_i), are listed in Table II. It is noted that the variation in the C_1 values is of the order of 6.83%, indicating that a single C_1 value will provide a good representation of the behavior of the flow. This general value of C_1 is found in the same fashion for all 13 sets of data by combining them into a single average set, as $C_1=0.645$. The numerically obtained $\theta_a(\tau)$ is plotted against $e^{-0.645(A\mathrm{Ra})^{-1/4}\tau}$ in Fig. 3(b) for all runs in Case 1, and the standard deviation (denotes as sd_t) produced by using this value of C_1 for each individual run is also listed in Table II, which clearly shows that this general value of C_1 gives a good quantification of the scaling relation (12) for A, Ra, and Pr in the ranges of $1/3 \leqslant A \leqslant 3$, $6\times 10^6 \leqslant \mathrm{Ra} \leqslant 6\times 10^{10}$, and $1 \leqslant \mathrm{Pr} \leqslant 1000$, that is,

$$\theta_a(\tau) = e^{-0.645(A\mathrm{Ra})^{-1/4}\tau} - 1. \tag{21}$$

The scaling and numerical results show that the time to full cooling, τ_f as defined above, scales as

$$\tau_f \sim (A\mathrm{Ra})^{1/4}. \tag{22}$$

Using the definition given above for τ_f, that is the time for $\theta_a(\tau)$ to reach -0.99, and the scaling relation (21), the scaled τ_f is obtained for Case 1 as

$$\tau_f = 7.140(A\mathrm{Ra})^{1/4}. \tag{23}$$

This τ_f will be used below to scale the Nusselt number and to obtain a time averaged Nusselt number.

The numerical results showing the dependence of the average Nusselt numbers on individual Ra, A, and Pr are presented in Fig. 4 for Case 1, where $\overline{\mathrm{Nu}}_{s,a}$ is the average Nusselt number on the side wall over τ_f, that is,

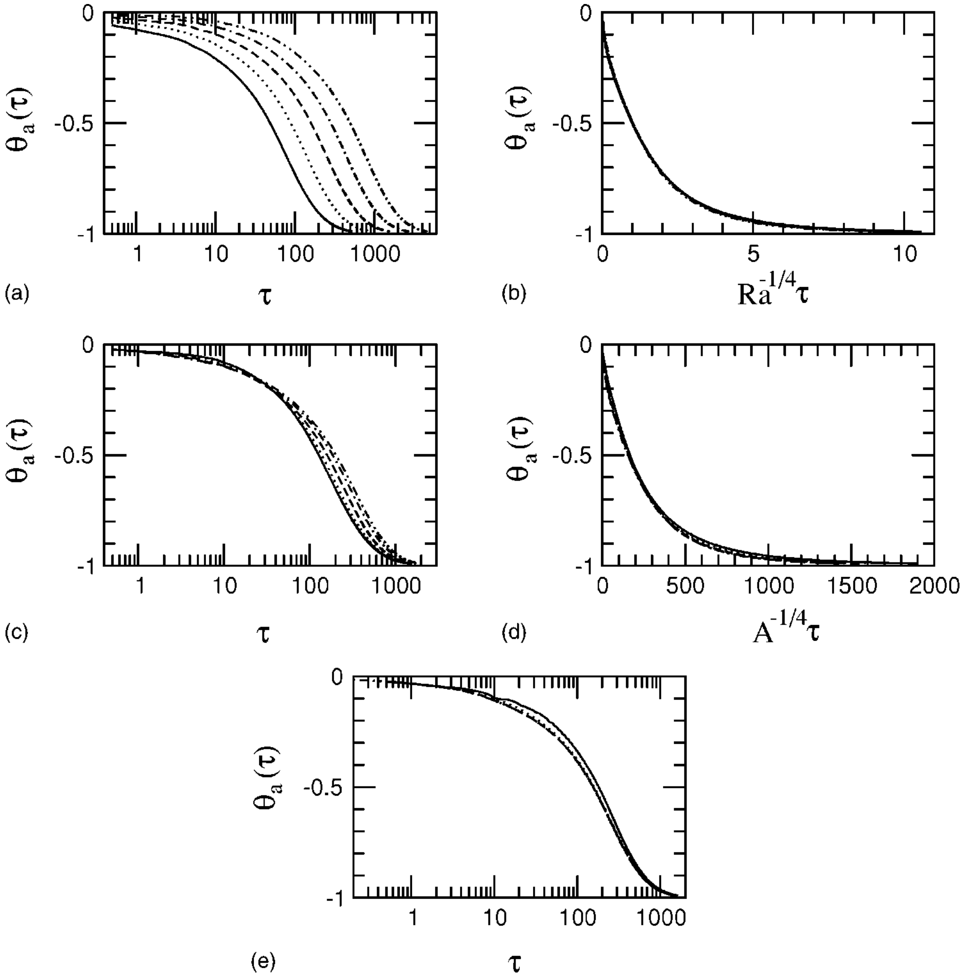

FIG. 2. (a) Time series of $\theta_a(\tau)$ and (b) $\theta_a(\tau)$ plotted against $\mathrm{Ra}^{-1/4}\tau$ for $\mathrm{Ra}=6\times10^6$ (—), 6×10^7 (⋯⋯), 6×10^8 (– – –), 6×10^9 (–·–), and 6×10^{10} (–··–) with $A=1$ and $\mathrm{Pr}=7$; (c) Time series of $\theta_a(\tau)$ and (d) $\theta_a(\tau)$ plotted against $A^{-1/4}\tau$ for $A=1/3$ (—), 1/2 (⋯⋯), 1 (– – –), 2 (–·–), and 3 (–··–) with $\mathrm{Ra}=6\times10^8$ and $\mathrm{Pr}=7$; (e) Time series of $\theta_a(\tau)$ for $\mathrm{Pr}=1$ (—), 7 (⋯⋯), 50 (– – –), 200 (–·–), and 1000 (–··–) with $\mathrm{Ra}=6\times10^8$ and $A=1$, respectively. All results are presented for Case 1.

$$\overline{\mathrm{Nu}}_{s,a}=\frac{1}{\tau_f}\int_0^{\tau_f}\overline{\mathrm{Nu}}_s(\tau)d\tau. \tag{24}$$

The time shown is scaled against τ_f, while the $\overline{\mathrm{Nu}}_s$ shown in (a) and (c) are scaled against $\mathrm{Ra}^{1/4}$ and $A^{3/4}$, respectively. It is apparent that the time scaling combined with the Ra and A scalings provides a good representation of the behavior of $\overline{\mathrm{Nu}}_s$, with all results collapsing close to single lines, in both (a) and (c). The Prandtl number variation results, shown in (e), again show that the Prandtl number is not an important control parameter, as predicted. The $\overline{\mathrm{Nu}}_s$ variation also shows

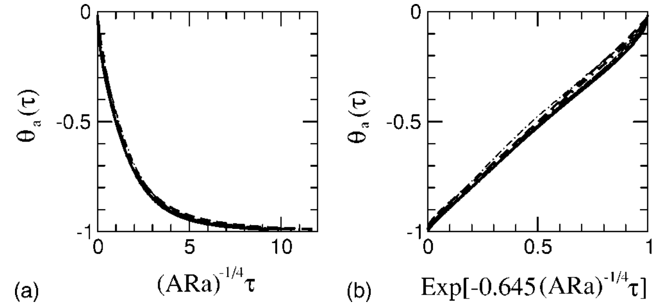

FIG. 3. $\theta_a(\tau)$ plotted against (a) $(A\mathrm{Ra})^{-1/4}\tau$ and (b) $e^{-0.645(A\mathrm{Ra})^{-1/4}\tau}$ for all simulations in Case 1. ——, $\mathrm{Ra}=6\times10^6$, $A=1$, $\mathrm{Pr}=7$; ⋯⋯, $\mathrm{Ra}=6\times10^7$, $A=1$, $\mathrm{Pr}=7$; – – –, $\mathrm{Ra}=6\times10^8$, $A=1$, $\mathrm{Pr}=7$; – – –, $\mathrm{Ra}=6\times10^9$, $A=1$, $\mathrm{Pr}=7$; –·–·–, $\mathrm{Ra}=6\times10^{10}$, $A=1$, $\mathrm{Pr}=7$; –·–·–, $\mathrm{Ra}=6\times10^8$, $A=1$, $\mathrm{Pr}=1$; –··–··–, $\mathrm{Ra}=6\times10^8$, $A=1$, $\mathrm{Pr}=50$; ––·–––·––, $\mathrm{Ra}=6\times10^8$, $A=1$, $\mathrm{Pr}=200$; ⋯⋯ (bold), $\mathrm{Ra}=6\times10^8$, $A=1$, $\mathrm{Pr}=1000$; – – – (bold), $\mathrm{Ra}=6\times10^8$, $A=1/3$, $\mathrm{Pr}=7$; –·–·– (bold), $\mathrm{Ra}=6\times10^8$, $A=1/2$, $\mathrm{Pr}=7$; –··–··–(bold), $\mathrm{Ra}=6\times10^8$, $A=2$, $\mathrm{Pr}=7$; —— (bold), $\mathrm{Ra}=6\times10^8$, $A=3$, $\mathrm{Pr}=7$.

TABLE II. Values of C_1 for each run and their corresponding standard deviations in Case 1.

Run	Ra	A	Pr	C_1	sd_i	sd_t
1	6×10^6	1	7	0.648	0.000766	0.000767
2	6×10^7	1	7	0.643	0.000514	0.000514
3	6×10^8	1	7	0.643	0.000355	0.000355
4	6×10^9	1	7	0.647	0.000260	0.000261
5	6×10^{10}	1	7	0.673	0.000263	0.000294
6	6×10^8	1/3	7	0.599	0.000357	0.000425
7	6×10^8	1/2	7	0.622	0.000341	0.000357
8	6×10^8	2	7	0.655	0.000519	0.000527
9	6×10^8	3	7	0.660	0.000517	0.000530
10	6×10^8	1	1	0.587	0.000245	0.000394
11	6×10^8	1	50	0.654	0.000393	0.000398
12	6×10^8	1	200	0.655	0.000392	0.000397
13	6×10^8	1	1000	0.655	0.000249	0.000251

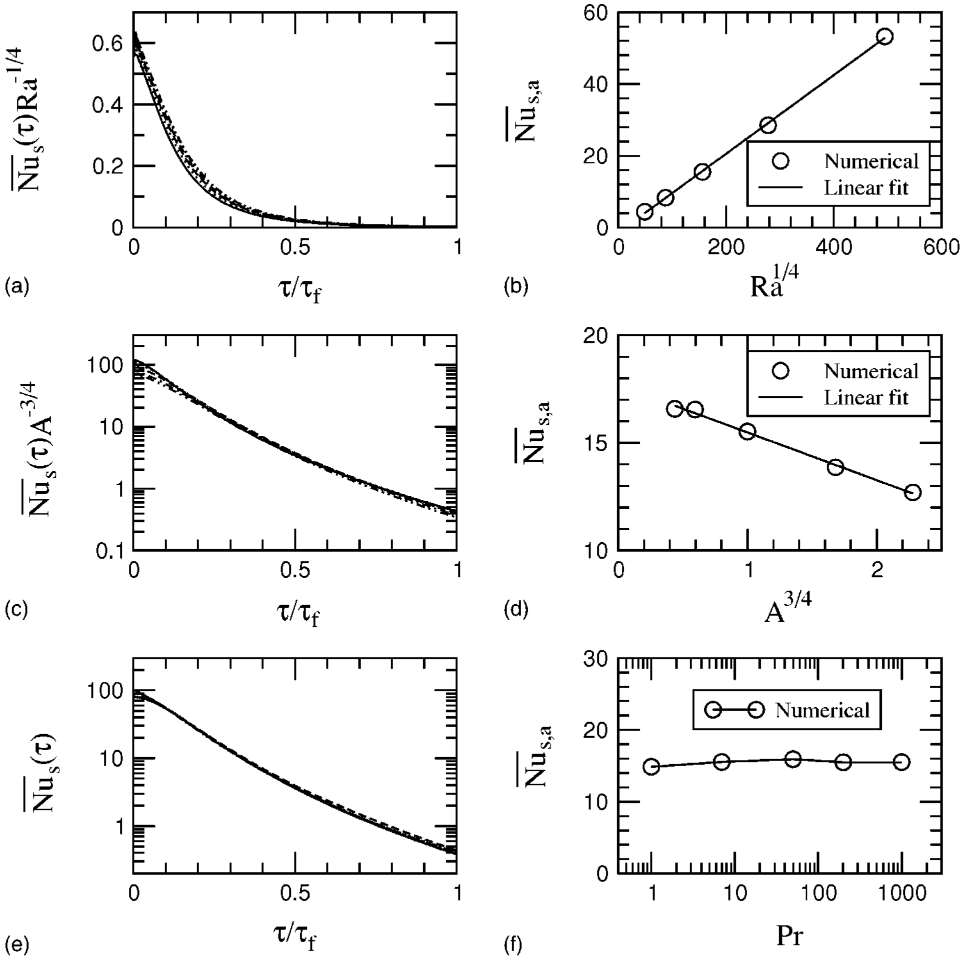

FIG. 4. (a) $\overline{\mathrm{Nu}}_s(\tau)\mathrm{Ra}^{-1/4}$ plotted against τ/τ_f and (b) $\overline{\mathrm{Nu}}_{s,a}$ plotted against $\mathrm{Ra}^{1/4}$ for $\mathrm{Ra}=6\times10^6$ (—), 6×10^7 (·····), 6×10^8 (– – –), 6×10^9 (–·–), and 6×10^{10} (–··–) with $A=1$ and $\mathrm{Pr}=7$; (c) $\overline{\mathrm{Nu}}_s(\tau)A^{-3/4}$ plotted against τ/τ_f and (d) $\overline{\mathrm{Nu}}_{s,a}$ plotted against $A^{3/4}$ for $A=1/3$ (—), $1/2$ (·····), 1 (– – –), 2 (-·-), and 3 (–··–) with $\mathrm{Ra}=6\times10^8$ and $\mathrm{Pr}=7$; (e) $\overline{\mathrm{Nu}}_s(\tau)$ plotted against τ/τ_f and (*f*) $\overline{\mathrm{Nu}}_{s,a}$ plotted against Pr for $\mathrm{Pr}=1$ (—), 7 (···), 50(– – –), 200 (-·-), and 1000 (–··–) with $\mathrm{Ra}=6\times10^8$ and $A=1$, respectively. All results are presented for in Case 1.

a basically asymptotic behavior, as expected, with relatively little variation over the last 60% of the development time. The time averaged results, shown in (b), (d), and (f), further confirm the $\overline{\mathrm{Nu}}_s$ scaling, showing very close to linear relations to $\mathrm{Ra}^{1/4}$ and $A^{3/4}$, and little variation with Pr.

It should be noted that the experimental results of Berkovsky and Polevikov [21] and the numerical results of Catton, Ayyaswamy, and Clever [22] show that $\overline{\mathrm{Nu}}_{s,a}$ has the following empirical dependence on both Ra and Pr for $2<A<10$, $\mathrm{Pr}<10^5$, and $\mathrm{Ra}<10^{10}$,

$$\overline{\mathrm{Nu}}_{s,a}=0.22A^{-1/4}\left(\frac{\mathrm{RaPr}}{0.2+\mathrm{Pr}}\right)^{0.28}. \tag{25}$$

This relation clearly shows that the Pr dependence of $\overline{\mathrm{Nu}}_{s,a}$ is only significant for $\mathrm{Pr}\sim1$. When Pr is large, the dependence of $\overline{\mathrm{Nu}}_{s,a}$ on Pr is negligible. The numerical results shown in Fig. 4(f) qualitatively show this feature. On the other hand, the scaling relation (11), which shows no dependence of $\overline{\mathrm{Nu}}_s$ on Pr, was developed with the assumption of Pr being larger than 1. When $\mathrm{Pr}\sim1$, such a scaling relation is not valid. It is expected that this will also be true for Case 2.

B. Case 2

The direct numerical simulation results for Case 2 are presented in Fig. 5 to show the individual dependence of the scaling relation (16) on Ra, *A*, and Pr, respectively. The collapse of all five sets of numerically obtained $\theta_a(\tau)$ onto a single curve in each of Figs. 5(b), 5(d), and 5(e) clearly shows that the dependence of the scaling relation (16) on each of the control parameters Ra, *A*, and Pr is true for Case 2, similar to that for Case 1.

The numerically obtained $\theta_a(\tau)$ is plotted against $(A\mathrm{Ra})^{-1/4}\tau$ in Fig. 6(a) for all runs in Case 2. The collapse of all sets of data onto a single curve confirms again that the scaling relation (16) is true for Case 2. The specific values of the proportional constant C_2 for each run, determined by the curve-fitting method with the minimal standard deviation sd_i, are listed in Table III. Once again a best fit single C_2 can be obtained for all the data, as described above, given for Case 2, $C_2=0.705$. All the data sets are plotted, using this C_2, in Fig. 6(b), while the standard deviation for each data set is shown in Table III as sd_t. The scaling relation (16) is therefore well approximated by the following general equation for *A*, Ra and Pr in the ranges of $1/3\leqslant A\leqslant3$, $6\times10^6\leqslant\mathrm{Ra}\leqslant6\times10^{10}$, and $1\leqslant\mathrm{Pr}\leqslant1000$,

$$\theta_a(\tau)=e^{-0.705(A\mathrm{Ra})^{-1/4}\tau}-1. \tag{26}$$

Using the definition given above for τ_f and the scaling relation (26), the scaled τ_f is obtained for Case 2 as

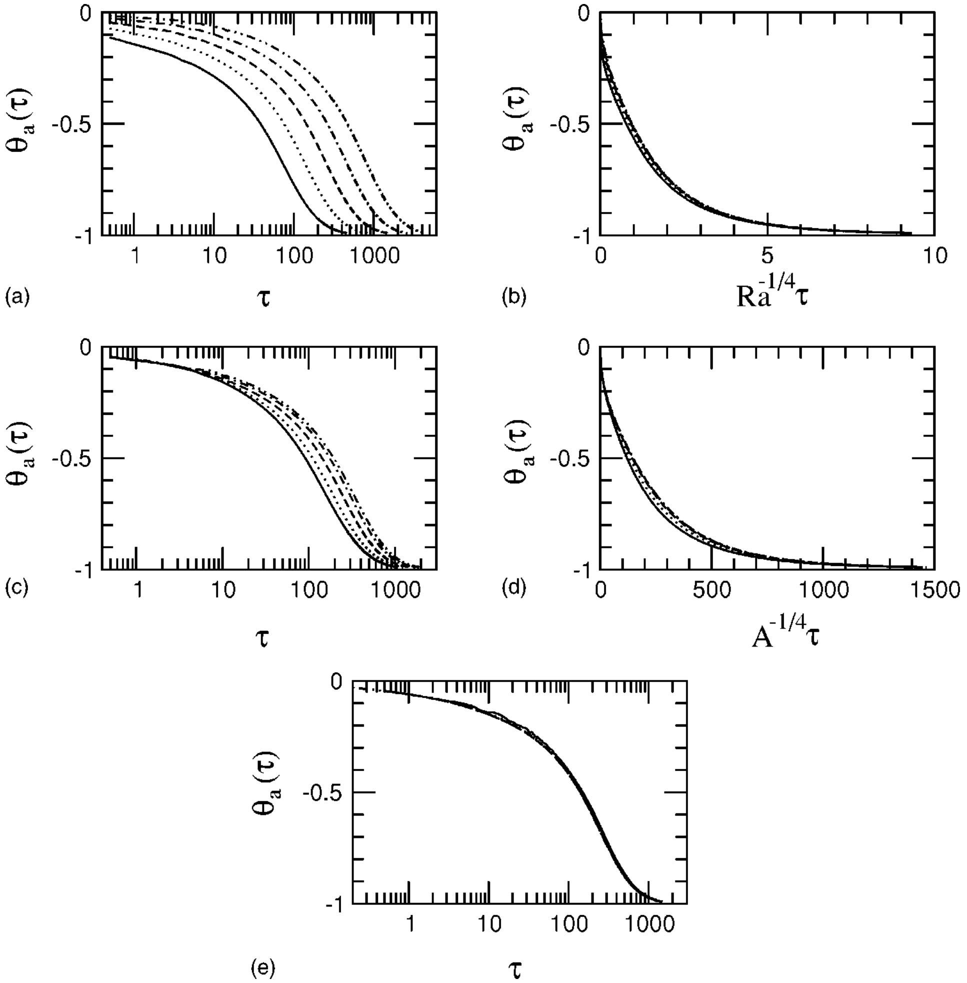

FIG. 5. (a) Time series of $\theta_a\tau$ and (b) $\theta_a(\tau)$ plotted against $\mathrm{Ra}^{-1/4}\tau$ for $\mathrm{Ra}=6\times10^6$ (—), 6×10^7 (·····), 6×10^8 (– – –), 6×10^9 (–·–), and 6×10^{10} (–··–) with $A=1$ and $\mathrm{Pr}=7$; (c) Time series of $\theta_a(\tau)$ and (d) $\theta_a(\tau)$ plotted against $A^{-1/4}\tau$ for $A=1/3$ (—), $1/2$ (·····), 1 (– – –), 2 (–·–), and 3 (–··–) with $\mathrm{Ra}=6\times10^8$ and $\mathrm{Pr}=7$; (e) Time series of $\theta_a(\tau)$ for $\mathrm{Pr}=1$ (—), 7 (… …), 50 (– – –), 200 (–·–), and 1000 (–··–) with $\mathrm{Ra}=6\times10^8$ and $A=1$, respectively. All results are presented for Case 2.

$$\tau_f = 6.532(A\mathrm{Ra})^{1/4}. \tag{27}$$

This τ_f will be used below to scale the Nusselt number and to obtain a time averaged Nusselt number.

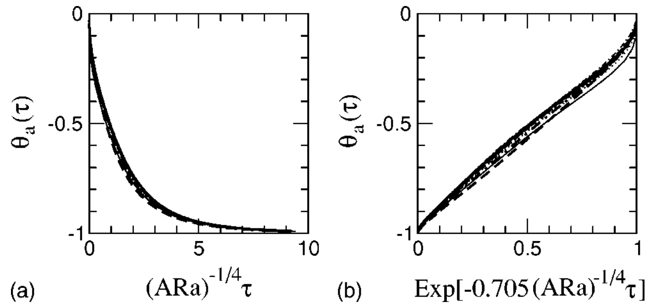

FIG. 6. $\theta_a(\tau)$ plotted against (a) $(A\mathrm{Ra})^{-1/4}\tau$ and (b) $e^{-0.705(A\mathrm{Ra})^{-1/4}\tau}$ for all simulations in Case 2. —, $\mathrm{Ra}=6\times10^8$, $A=1$, $\mathrm{Pr}=7$; ·····, $\mathrm{Ra}=6\times10^7$, $A=1$, $\mathrm{Pr}=7$; ----, $\mathrm{Ra}=6\times10^8$, $A=1$, $\mathrm{Pr}=7$; – – –, $\mathrm{Ra}=6\times10^9$, $A=1$, $\mathrm{Pr}=7$; –·–·–, $\mathrm{Ra}=6\times10^{10}$, $A=1$, $\mathrm{Pr}=7$; –·–·–, $\mathrm{Ra}=6\times10^8$, $A=1$, $\mathrm{Pr}=1$; –··–··–, $\mathrm{Ra}=6\times10^8$, $A=1$, $\mathrm{Pr}=50$; ––·–––·––, $\mathrm{Ra}=6\times10^8$, $A=1$, $\mathrm{Pr}=200$; ······ (bold), $\mathrm{Ra}=6\times10^8$ $A=1$, $\mathrm{Pr}=1000$; –––– (bold), $\mathrm{Ra}=6\times10^8$, $A=1/3$, $\mathrm{Pr}=7$; –·–·– (bold), $\mathrm{Ra}=6\times10^8$ $A=1/2$, $\mathrm{Pr}=7$; –··–··–(bold), $\mathrm{Ra}=6\times10^8$, $A=2$, $\mathrm{Pr}=7$; — (bold), $\mathrm{Ra}=6\times10^8$, $A=3$, $\mathrm{Pr}=7$.

The numerical results showing the dependence of the average Nusselt numbers on Ra, A and Pr are presented in Figs. 7–9 for Case 2 respectively, where $\overline{\mathrm{Nu}}_{b,a}$ is the average Nusselt number on the bottom boundary over τ_f and $\overline{\mathrm{Nu}}_{t,a}$ is the average Nusselt number on all boundaries, that is,

TABLE III. Values of C_2 for each run and their corresponding standard deviations in Case 2.

Run	Ra	A	Pr	C_2	sd_i	sd_t
1	6×10^6	1	7	0.771	0.001275	0.001379
2	6×10^7	1	7	0.724	0.00806	0.000815
3	6×10^8	1	7	0.697	0.000525	0.000527
4	6×10^9	1	7	0.685	0.000352	0.000360
5	6×10^{10}	1	7	0.704	0.000363	0.000363
6	6×10^8	1/3	7	0.798	0.000652	0.000814
7	6×10^8	1/2	7	0.740	0.000590	0.000616
8	6×10^8	2	7	0.681	0.000669	0.000687
9	6×10^8	3	7	0.679	0.000631	0.000652
10	6×10^8	1	1	0.670	0.000486	0.000516
11	6×10^8	1	50	0.703	0.000537	0.000537
12	6×10^8	1	200	0.706	0.000541	0.000541
13	6×10^8	1	1000	0.706	0.000344	0.000344

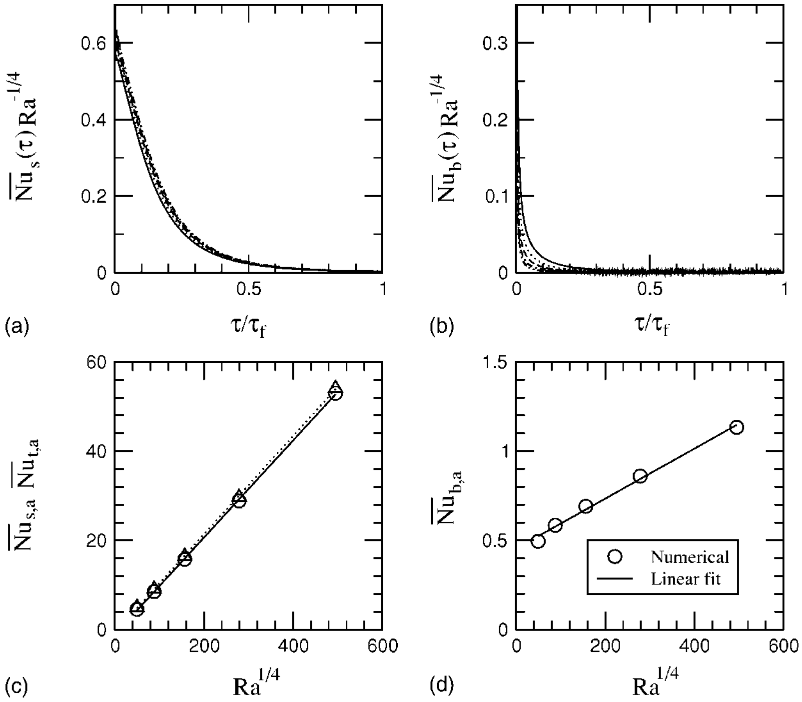

FIG. 7. (a) $\overline{\mathrm{Nu}}_s(\tau)\mathrm{Ra}^{-1/4}$ and (b) $\overline{\mathrm{Nu}}_b(\tau)\mathrm{Ra}^{-1/4}$ plotted against τ/τ_f for $\mathrm{Ra}=6\times10^6$ (—), 6×10^7 (·····), 6×10^8 (–––), 6×10^9 (–·–), and 6×10^{10} (–··–), (c) $\overline{\mathrm{Nu}}_{s,a}$ and $\overline{\mathrm{Nu}}_{t,a}$ and (d) $\overline{\mathrm{Nu}}_{b,a}$ plotted against $\mathrm{Ra}^{1/4}$ with $A=1$ and $\mathrm{Pr}=7$ in Case 2. ○ and △ in (c) are numerical data for $\overline{\mathrm{Nu}}_{s,a}$ and $\overline{\mathrm{Nu}}_{t,a}$, and — and ····· are their corresponding linear fit curves, respectively.

$$\overline{\mathrm{Nu}}_{b,a}=\frac{1}{\tau_f}\int_0^{\tau_f}\overline{\mathrm{Nu}}_b(\tau)d\tau, \tag{28}$$

and

$$\overline{\mathrm{Nu}}_{t,a}=\overline{\mathrm{Nu}}_{b,a}+\overline{\mathrm{Nu}}_{s,a}. \tag{29}$$

The time shown is scaled against τ_f, while the $\overline{\mathrm{Nu}}_s$ shown in Fig. 7(a) and $\overline{\mathrm{Nu}}_b$ shown in Fig. 7(b) are scaled against $\mathrm{Ra}^{1/4}$, and the $\overline{\mathrm{Nu}}_b$ shown in Fig. 8(a) is scaled against $A^{3/4}$, respectively. It is apparent that the time scaling combined with the Ra and A scalings provides a good representation of the behavior of $\overline{\mathrm{Nu}}_s$ for Case 2, with all results collapsing close to single lines, in both Figs. 7(a) and 8(a). The time scaling combined with the Ra and A scalings provides less satisfactory representation of the behavior of $\overline{\mathrm{Nu}}_b$, with some variations seen in the results shown in both Figs. 7(b) and 8(b). The time averaged results, shown in Figs. 7(c) and 8(c), further confirm the $\overline{\mathrm{Nu}}_s$ scalings, showing very close to linear relations to $\mathrm{Ra}^{1/4}$ and $A^{3/4}$. The results for $\overline{\mathrm{Nu}}_{b,a}$ show a linear

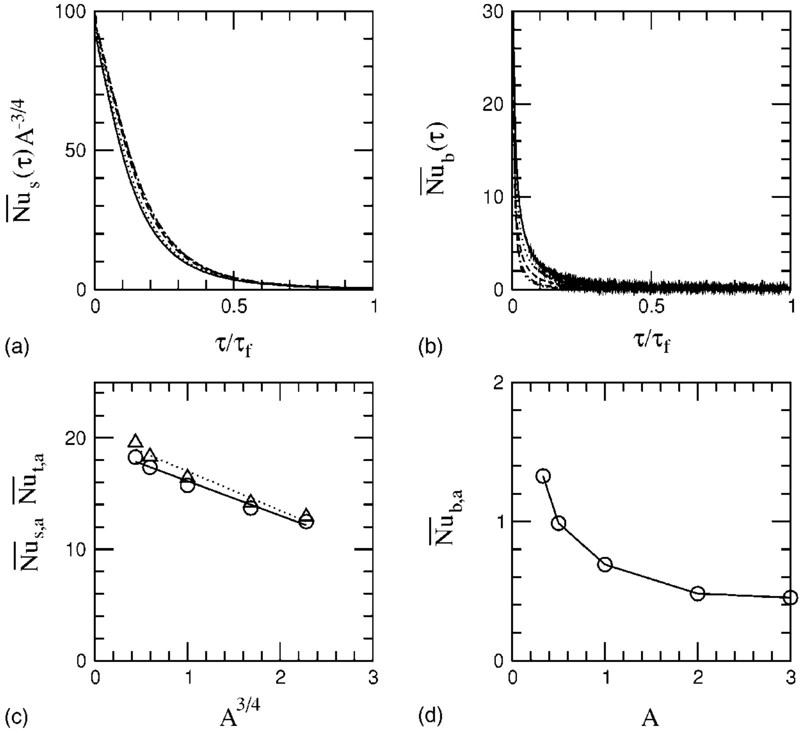

FIG. 8. (a) $\overline{\mathrm{Nu}}_s(\tau)A^{-3/4}$ and (b) $\overline{\mathrm{Nu}}_b(\tau)$ plotted against τ/τ_f for $A=1/3$(—), $1/2$(·····), 1(–––), 2(–·–), and 3(–··–), (c) $\overline{\mathrm{Nu}}_{s,a}$ and $\overline{\mathrm{Nu}}_{t,a}$ plotted against $A^{3/4}$ and (d) $\overline{\mathrm{Nu}}_{b,a}$ plotted against A with $\mathrm{Ra}=6\times10^8$ and $\mathrm{Pr}=7$ in Case 2. ○ and △ in (c) are numerical data for $\overline{\mathrm{Nu}}_{s,a}$ and $\overline{\mathrm{Nu}}_{t,a}$, and — and ····· are their corresponding linear fit curves, respectively.

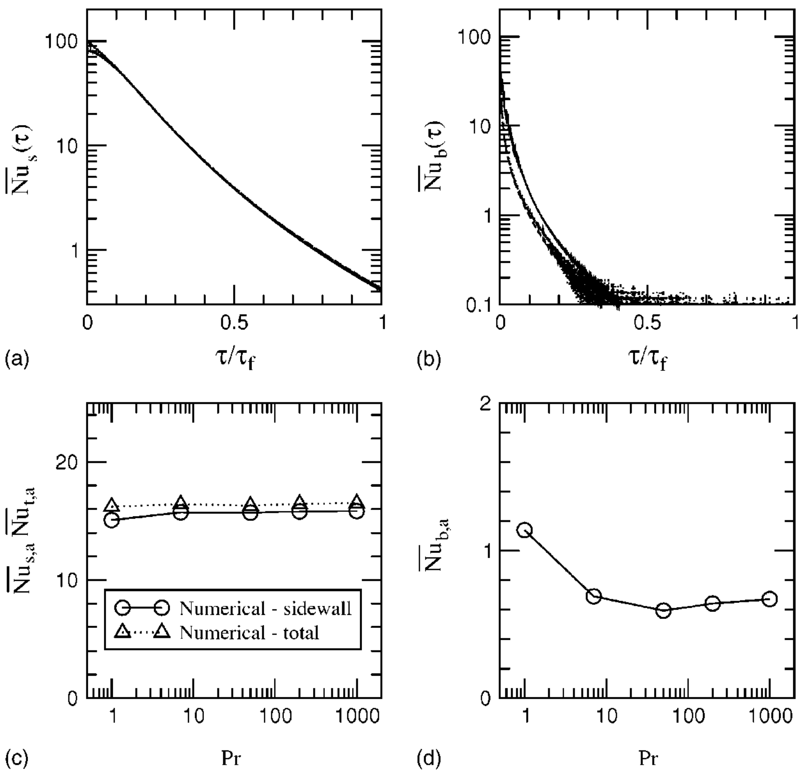

FIG. 9. (a) $\overline{\mathrm{Nu}}_s(\tau)$ and (b) $\overline{\mathrm{Nu}}_b(\tau)$ plotted against τ/τ_f for Pr=1(—), 7(·····), 50(– – –), 200 (–·–), and 1000 (–· ·–) (c) $\overline{\mathrm{Nu}}_{s,a}$ and $\overline{\mathrm{Nu}}_{t,a}$ and (d) $\overline{\mathrm{Nu}}_{b,a}$ plotted against Pr with $\mathrm{Ra}=6\times10^8$ and $A=1$ in Case 2.

relation with $\mathrm{Ra}^{1/4}$, as shown in Fig. 7(d), however the A scaling, shown in Fig. 8(d), shows some nonlinear behavior for low A. The $\overline{\mathrm{Nu}}_{t,a}$ results show linear relation with $\mathrm{Ra}^{1/4}$ and $A^{3/4}$. The numerical results showing the dependence of the average Nusselt numbers on Pr for Case 2, as presented in Fig. 9, clearly show that there is relatively little dependence on Pr for the long-term behavior of $\overline{\mathrm{Nu}}_s$, $\overline{\mathrm{Nu}}_{s,a}$, and $\overline{\mathrm{Nu}}_{t,a}$, again consistent with the assumption about the average heat transfer coefficient on the side wall. The $\overline{\mathrm{Nu}}_b$ and $\overline{\mathrm{Nu}}_{,a}$ relations are less satisfactory, showing some Pr dependence in the heat transfer on the bottom boundary.

The percentage of heat transferred through the bottom boundary over τ_f, ϕ_b, is defined as

$$\phi_b = \frac{\int_0^{\tau_f} \overline{h_b} A_b d\tau}{\int_0^{\tau_f} \overline{h_b} A_b d\tau + \int_0^{\tau_f} \overline{h_s} A_s d\tau}, \qquad (30)$$

which can also be expressed as follows

$$\phi_b = \frac{\overline{\mathrm{Nu}}_{b,a}}{\overline{\mathrm{Nu}}_{b,a} + \overline{\mathrm{Nu}}_{s,a}}. \qquad (31)$$

The numerically obtained ϕ_b is presented in Table IV for all runs in Case 2, clearly showing that the assumption $\overline{h_b} \ll \overline{h_s}$ which was made in the scaling analysis is true.

It is clear that the heat transfer occurs primarily on the side walls and will be associated with the convective boundary layer that forms there. The flow velocity adjacent to the bottom boundary will be relatively small, particularly during the later stages of cooling, and the heat transfer in that region will be considerably less than that on the side wall.

V. CONCLUDING REMARKS

Scaling analysis has been used to obtain time scales for the long-term behavior of the cooling of a fluid in a rectangular container with an infinite length via the side walls and the side wall and bottom. The scaling relations have been validated by comparison to numerical simulation. The numerical results have also been used to obtain the proportionality constants in the scaling relations, allowing the time re-

TABLE IV. Numerical results of ϕ_b for all simulations in Case 2.

Run	Ra	A	Pr	ϕ_b (%)
1	6×10^6	1	7	9.86
2	6×10^7	1	7	6.55
3	6×10^8	1	7	4.20
4	6×10^9	1	7	2.90
5	6×10^{10}	1	7	2.10
6	6×10^8	1/3	7	6.77
7	6×10^8	1/2	7	5.38
8	6×10^8	2	7	3.39
9	6×10^8	3	7	3.50
10	6×10^8	1	1	7.02
11	6×10^8	1	50	3.64
12	6×10^8	1	200	3.90
13	6×10^8	1	1000	4.24

quired for cooling to any required degree to be accurately determined.

Using 99% as the cool down criterion the scaled nondimensional cool down time for the side cooled cavity is 7.140 $(A\mathrm{Ra})^{1/4}$, and for the side and bottom cooled cavity is 6.532 $(A\mathrm{Ra})^{1/4}$. It has been shown that for Case 1, side wall cooling only, the scaling relations correspond very well to the behavior of the numerical results, confirming the approximations used to obtain those relations. The results for Case 2 also show that the scaling relations provide a very good prediction of the overall cooling down rate, represented as $\theta_a(\tau)$. The form of the $\theta_a(\tau)$ scaling relation for Case 2 is the same as that for Case 1, with only a variation in the proportionality constant, as noted above. This again confirms that the assumptions made in obtaining the scaling relations are correct, and that additionally cooling the bottom has little effect on the overall cooling rate. The relative behavior of the bottom and side wall cooling has been further investigated by obtaining $\overline{\mathrm{Nu}}_s$ and $\overline{\mathrm{Nu}}_b$ separately, and comparing them to their scaling relations. $\overline{\mathrm{Nu}}_s$ is seen to correspond very well to the scaling relation, while the $\overline{\mathrm{Nu}}_b$ correspondence is seen to be less satisfactory, with some Pr dependence observed as well as some variations observed in the scaled results. This may be, at least in part, attributed to the variation in the nature of the heat transfer within the fluid adjacent to the bottom boundary. In the early stages of the flow an intrusion travels from the wall across the container bottom, and during that stage the $\overline{\mathrm{Nu}}_b$ heat transfer is relatively large, as seen in Figs. 7(b), 8(b), and 9(b), however during the later stages of cooling the flow adjacent to the bottom is near to quiescent and the predominant mode of heat transfer within the fluid in that region is conduction. The observation that $\overline{\mathrm{Nu}}_b$ has some Pr dependence supports this hypothesis, however the scaling relations do not represent this change in flow type, or the weak Pr dependence.

Despite this, the overall heat transfer rate for Case 2 is well represented by the scaling relations, as seen in the $\overline{\mathrm{Nu}}_{t,a}$ results, and this is at least in part because this is dominated by $\overline{\mathrm{Nu}}_{s,a}$. The side wall heat transfer is predominantly a result of the natural convection boundary layer which forms there, maintaining a high-temperature gradient throughout the cooling process. The overall heat transfer and cooling process for Case 2 is therefore dominated by the side wall heat transfer, and as a result, for both Case 1 and 2 the cooling rate and total heat transfer are well represented by the scaling relations presented above.

ACKNOWLEDGMENTS

The financial support of the Australian Research Council, (Grant No. DP0449876) from the National Natural Science Foundation of China (Grant No. 10262003), and the Natural Science Foundation of Yunnan Province of China (Key Project Grant No. 2003E0004Z), are gratefully acknowledged.

---

[1] I. Catton, in *Proceedings of the 6th International Heat Transfer Conference*, edited by U. Grigull *et al.* (Hemisphere, Washington, 1978), Vol. 6, pp. 13–43; S. Ostrach, in *Proceedings of the 7th International Heat Transfer Conference*, edited by U. Grigull *et al.* (Hemisphere, Washington, 1982), Vol. 1, pp. 365–379; B. Gebhart *et al.*, *Buoyancy-Induced Flows and Transport* (Hemisphere, New York, 1988); J. M. Hyun, Adv. Heat Transfer **24**, 277 (1994).
[2] R. J. Goldstein *et al.*, Int. J. Heat Mass Transfer **46**, 1887 (2003).
[3] T. Sakurai and T. Matsuda, J. Fluid Mech. **54**, 417 (1972).
[4] M. C. Jischke and R. T. Doty, J. Fluid Mech. **71**, 729 (1975).
[5] J. M. Hyun, W. W. Fowlis, and A. Warn-Varnas, J. Fluid Mech. **117**, 71 (1982); J. M. Hyun, ASME J. Appl. Mech. **52**, 193 (1985); J. M. Hyun and H. K. Choi, J. Thermophys. Heat Transfer **3**, 441 (1989).
[6] J. C. Patterson and J. Imberger, J. Fluid Mech. **100**, 65 (1980).
[7] J. M. Hyun, Int. J. Heat Mass Transfer **27**, 1936 (1984); **107**, 982 (1985).
[8] V. F. Nicolette and K. T. Yang, Int. J. Heat Mass Transfer **28**, 1721 (1985).
[9] D. R. Otis and J. Roessler, Int. J. Heat Mass Transfer **30**, 1633 (1987).
[10] S. G. Schladow, J. C. Patterson, and R. L. Street, J. Fluid Mech. **200**, 121 (1989).
[11] J. C. Patterson and S. W. Armfield, J. Fluid Mech. **219**, 469 (1990).
[12] S. W. Armfield and J. C. Patterson, Int. J. Heat Mass Transfer **34**, 929 (1991); J. Fluid Mech. **239**, 195 (1992); S. W. Armfield and R. Janssen, Int. J. Heat Fluid Flow **17**, 539 (1996).
[13] S. Xin and P. Le Quéré, J. Fluid Mech. **304**, 87 (1995).
[14] A. M. H. Brooker, J. C. Patterson, and S. W. Armfield, J. Fluid Mech. **352**, 265 (1997).
[15] H. S. Kwak, K. Kuwahara, and J. M. Hyun, Int. J. Heat Mass Transfer **41**, 323 (1998).
[16] W. Lin and S. W. Armfield, Int. J. Heat Mass Transfer **42**, 4117 (1999).
[17] W. Lin, Ph.D. thesis, The University of Sydney, Sydney, 2000 (unpublished).
[18] W. Lin and S. W. Armfield, Int. J. Heat Fluid Flow **22**, 72 (2001).
[19] W. Lin, S. W. Armfield, and P. L. Morgan, Int. J. Heat Mass Transfer **45**, 451 (2002).
[20] R. D. C. Oliveski, A. Krenzinger, and H. A. Vielmo, Int. J. Heat Mass Transfer **46**, 2015 (2003).
[21] B. M. Berkovsky and V. K. Polevikov, in *Heat Transfer and Turbulent Buoyant Convection*, edited by D. B. Spalding and H. Afghan (Hemisphere, Washington, 1977).
[22] I. Catton, P. S. Ayyaswamy, and R. M. Clever, Int. J. Heat Mass Transfer **17**, 173 (1974).
[23] B. P. Leonard, Comput. Methods Appl. Mech. Eng. **19**, 59 (1979).

[24] S. W. Armfield, Comput. Fluids **20**, 1 (1991); S. W. Armfield and R. L. Street, J. Comput. Phys. **153**, 660 (1999).

[25] S. W. Armfield and W. Debler, Int. J. Heat Mass Transfer **36**, 519 (1993); A. Javam, J. Imberger, and S. W. Armfield, J. Fluid Mech. **396**, 183 (1999).

[26] W. Lin and S. W. Armfield, Phys. Rev. E **66**, 066308 (2002); J. Fluid Mech. **403**, 67 (2000); Int. J. Heat Mass Transfer **43**, 3013 (2000); Comput. Mech. **31**, 379 (2003); Numer. Heat Transfer, Part A **38**, 377 (2000); Energy **23**, 719 (1998).